

Document downloaded from:

<http://hdl.handle.net/10251/194636>

This paper must be cited as:

Pascual García, J.; Rubio Arjona, L.; Rodrigo Peñarrocha, VM.; Juan-Llácer, L.; Molina-García-Pardo, JM.; Sanchis-Borrás, C.; Reig, J. (2022). Wireless Channel Analysis Between 25 and 40 GHz in an Intra-Wagon Environment for 5G Using a Ray-Tracing Tool. IEEE Transactions on Intelligent Transportation Systems. 23(12):24621-24635.  
<https://doi.org/10.1109/TITS.2022.3199159>



The final publication is available at

<https://doi.org/10.1109/TITS.2022.3199159>

Copyright Institute of Electrical and Electronics Engineers

Additional Information

# Wireless Channel Analysis between 25 and 40 GHz in an Intra-Wagon Environment for 5G using a Ray-Tracing tool

Juan Pascual-García, *Member, IEEE*, Lorenzo Rubio, *Senior Member, IEEE*, Vicent M. Rodrigo Peñarrocha, Leandro Juan-Llácer, *Senior Member, IEEE*, José-María Molina-García-Pardo, Concepción Sanchis-Borras, and Juan Reig, *Senior Member, IEEE*

**Abstract**— Metro and railway systems are one of the most used transportation systems for people in almost all countries. Nevertheless, the access to high throughput wireless services is still very limited inside the wagons (cars). A deep analysis of the wireless channel inside wagons is needed to deploy new efficient and high throughput networks as the ones provided by fifth-generation (5G) systems. Although several works have analyzed the intra-wagon channel, some limitations are usually present: only certain user equipment-access point situations were considered, the number of studied propagation mechanisms was limited, and only some channel parameters were extracted. For these reasons, in this work the wireless channel in an intra-wagon environment is thoroughly analyzed using simulations performed with a ray-tracing tool calibrated and validated with wideband measurements. Thanks to the accurate ray-tracing tool the main replicas are identified in different typical user equipment-access point positions; the contribution of each propagation mechanism to the total power is extracted; and the angular spread in azimuth and elevation for the direction of arrival and departure are obtained. This analysis is performed in the frequency range from 25 to 40 GHz, where spectrum for several 5G bands has been already allocated.

**Index Terms**—5G, intra-wagon, mm-Wave, channel simulation, ray-tracing.

## I. INTRODUCTION

**M**ETRO and railway wagons (cars) constitute one of the most challenging scenarios for the deployment of high capacity wireless and mobile communications systems [1]-[3]. Densities as high as 5 persons/m<sup>2</sup> can be reached [4]; moreover, the confined structure and the

presence of many metallic objects produce a very rich multipath channel [5]. Additionally, the new low millimeter wave (mm-Wave) bands, reserved for 5G systems in the World Radio Conferences held in 2015 [6] and 2019 [7], have been in general least analyzed than the well-known sub-6 GHz bands. For all these reasons, the wireless channel must be thoroughly studied in the mentioned environment at the new bands.

Few works have measured and analyzed the intra-wagon channel. The particular structure of the environment produces both long delay and relatively high-power replicas, which requires a careful selection of time and frequency parameters in the measurement setup to avoid artifacts; in addition, the wagons are usually available for scientists for a limited time which in turn limits the number of measurements. The presence of clusters was studied in the 26.5–40 GHz band in [4] and [8]; additionally, in [8] the clusters were used to obtain the Saleh-Valenzuela parameters. The path loss models have been estimated in different bands; we can mention the comparison between the ITU-R path loss model for non-line-of-sight indoor hotspot scenarios (ITU-R M.2135-1) and the estimated path loss model performed at 5 GHz for intra-train communications links in [9]; narrowband measurements were carried out at 2.6 GHz to estimate the parameters of the path loss model in links for the train control and management system in [10]; at low mm-Wave bands we can find the results obtained for the band 26.5–40 GHz in [4] and the path loss models for different sub-bands between 25 and 40 GHz in [5]. One of the most critical parameters is the root mean square of the delay spread (RMS DS), which is usually extracted from the power delay profile (PDP); thus, in [5] the

This work was supported by the Ministerio de Ciencia e Innovación of the Spanish Government under the National Projects PID2019-107885GB-C33, and PID2020-119173RB-C21 through the Agencia Estatal de Investigación (AEI) and the Fondo Europeo de Desarrollo Regional (FEDER).

(Corresponding author: Juan Pascual-García)

J. Pascual-García, L. Juan-Llácer, and J.-M. Molina-García-Pardo are with Information Technologies and Communications Department, Universidad Politécnica de Cartagena, 30202 Cartagena,

Spain (e-mail: juan.pascual@upct.es, josemaria.molina@upct.es; leandro.juan@upct.es).

L. Rubio, V. M. Rodrigo Peñarrocha, and J. Reig are with iTEAM Research Institute, Universitat Politècnica de València, 46022 Valencia, Spain (e-mail: lrubio@dcom.upv.es; vrodrigo@dcom.upv.es; jreig@dcom.upv.es).

C. Sanchis-Borras is with the Department of Technical Sciences, Universidad Católica San Antonio de Murcia, 30107 Murcia, Spain (e-mail: csanchis@ucam.edu).

RMS DS was estimated for different low mm-Wave sub-bands whereas in [10] the RMS DS and the angle of arrival were extracted at 2.6 GHz from wideband measurements. Finally, distinct multiple-input multiple-output (MIMO) configurations and the contribution of dense multipath components were analyzed between 25 and 40 GHz in [11] and [12], respectively.

Channel simulators are useful tools in the design, deployment, and test of wireless systems, avoiding continuous measurement campaigns, which can be expensive and time-consuming. Among the different simulation tools, ray-tracing techniques achieve high levels of accuracy spending a reasonable amount of computer resources and simulation time [13]. Furthermore, ray-tracing techniques can extract relevant channel parameters that are of difficult estimation from measurements, as for instance the angles of arrival and departure. As in the measurements case, to the best of the authors' knowledge, few works have used these tools to analyze the intra-wagon environment. In [14] the RMS DS and angular spread (AS) are obtained in the 29.5 GHz band in a railway train intra-wagon scenario. In [15] ray-tracing simulations were validated with measurements carried out in a railway train wagon at 60 and 300 GHz bands; moreover, the simulator was used to analyze thoroughly the wireless channel. A ray-tracing tool, including diffuse scattering, was combined with a graph channel model in [16] to study the intra-wagon channel in a metro convoy; the simulation tool was tuned using simulations performed between 26.5 and 40 GHz. In [17], a ray tracer was used to study the influence of typical railway objects in intra-wagon communications and specially in train-to-infrastructure railway communications scenarios.

The mentioned works found in the literature present some significant limitations. In [14] and [17] the simulations are not compared with measurements. The user equipment (UE) location is usually restricted to the seated case as in [14]-[16]. Moreover, only polygons are used to represent the elements of the environment, even though cylindrical structures can be found inside a metro wagon; for example, in [16] the cylindrical shape of the handholds was approximated using rectangles. The order of the propagation mechanisms is usually limited, for example, in [15]-[16] the maximum order was set to two. Finally, some propagation mechanisms, such as diffractions in [16] and combinations of reflections and diffractions in [14]-[17], are absent in the simulations.

In this way, we have used a ray-tracing tool based on image theory in an intra-wagon environment of a metro convoy in the frequency range of 25–40 GHz to overcome the mentioned limitations, allowing a deeper insight into the wireless channel. The novelties and the most remarkable results of the paper are as follows:

- The simulation tool has been calibrated using

measurements.

- The maximum order of the propagation mechanisms has been set to three.

- The channel has been simulated for two different UE types of locations in the metro wagon: one imitating a passenger standing up in the central position of the corridor and one emulating a passenger seated. Moreover, different positions of the access point (AP) and UEs have been considered.

- To the best of the authors' knowledge this is the first time a deep analysis of the contribution of each propagation mechanism to the total power in an intra-wagon environment is performed.

- Appropriate formulations for reflection at curve shape handholds (poles) have been used.

- The main replicas have been identified using the capability of the simulation tool to trace the path of all involved rays.

- The angular characteristics have been analyzed quantitatively.

The paper is organized as follows. In Section II, the measurements are described. In Section III, the simulator is presented and the validation using the measurements is explained. The simulation results are shown in Section IV. Finally, the conclusions and future work are summarized in Section V.

## II. DESCRIPTION OF THE MEASUREMENTS

### A. Environment

The studied environment is an underground metro convoy of Ferrocarriles de la Generalitat Valenciana (FGV) in Valencia, Spain. The convoy is composed of four wagons that form a continuous train, with a small cabinet for the driver on both ends and several doors in each wagon. The total dimensions of the convoy are 55.25 m (length)  $\times$  2.55 m (width)  $\times$  2.15 m (height).

In Fig. 1 a picture of the environment and the transmitter (Tx) and receiver (Rx) antennas are shown. As seen in the picture, there are seats on each side, windows, handholds, and columns delimiting each door. Several materials are present in the convoy, with a predominance of metals. The floor is made of stratified rubber whereas the roof is made of stainless steel. The seats are resin-molded, reinforced with glass fiber, and the windows are made of laminated glass. The doors are made of aluminum, and they have two small windows made of glass. The handholds are made of stainless steel.

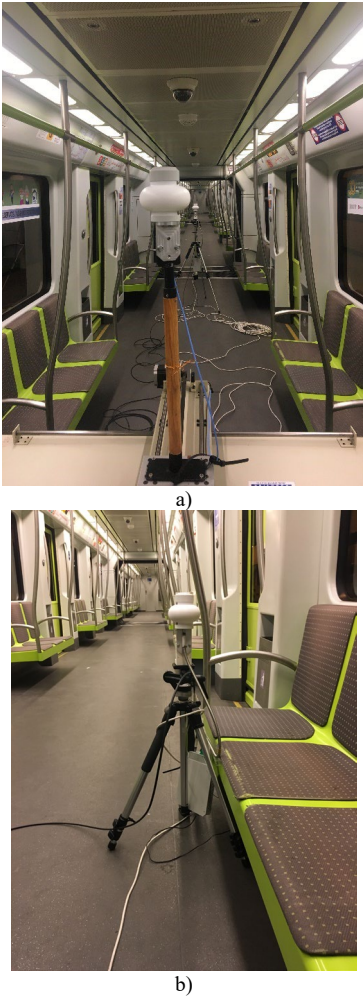


Fig. 1. Photograph of the metro convoy and the a) Rx antenna and b) Tx antenna.

### B. Measurement setup

The channel sounder is based on the Keysight PNA N5227 vector network analyzer (VNA) and a broadband radio over fiber (RoF) system. To collect all channel replicas of the channel, Q-PAR QOM-SL-0.8-40-K-SG-L ultra-wideband omnidirectional antennas were used at the Tx and Rx ends; vertical polarization was used in both ends. In order to measure large Tx-Rx distances and achieve enough dynamic range in all measurements, the Tx subsystem was connected to the VNA through the RoF link, which avoided the high losses of cables at mm-Wave frequencies. Moreover, the bandwidth of the intermediate frequency filter at the VNA was set to 100 Hz. Such value guaranteed an excellent trade-off between dynamic range (118 dB at 25 GHz) and acquisition time in the measurement.

Prior to all measurements a through calibration step was applied to the complete equipment excluding the antennas; as explained in [5] the calibration procedure is based on connecting the transmitter cable to the receiver cable using a transition, the calibration process moves the time reference points from the VNA ports to the calibration points by removing the effect of all cables and

amplifiers. Thus, the channel sounder measured the  $S_{21}(f)$  scattering parameter equivalent to the channel frequency transfer function  $H(f)$  including the antennas effect [18]. The number of frequency points was set to 8192, which corresponds to a frequency resolution  $\Delta f$  about 1.83 MHz; this value allows a maximum measurable path distance of 164 m, larger than the convoy length, thereby preventing the aliasing in the time domain. During the measurements, the convoy was parked away from other convoys and staff, and nobody was inside the convoy, guaranteeing stationary conditions. Additional details of the measurements can be found in [5].

### C. System configuration

The Rx was moved using an XY positioning system to implement a  $7 \times 7$  virtual rectangular array (URA). A personal computer controlled both the VNA and the XY positioning system. The separation between two consecutive URA elements was set to 3.04 mm, less than  $\lambda/2 = 3.7$  mm at 40 GHz. The Rx-URA was placed in two different positions imitating the position of an AP whereas the Tx antenna was manually placed in different locations along the convoy. The Tx imitates the position of a UE in two different situations, as explained in the introduction: a UE that travels standing in the central position of the corridor and a seated UE. The height of the Rx-URA was 1.63 m in all cases and the Tx height was set to 1.45 m for the standing UE positions and 0.85 m for the seated UE positions. All measured Tx-Rx positions were in line-of-sight (LoS) condition.

Different combinations of Rx-Tx positions were measured defining four scenarios as seen in Fig. 2. The details of the Rx-Tx positions can be found in [5] and [11]. In Fig. 3 the measured  $H(f)$  function at the central element of the virtual URA is shown for one position in each one of the scenarios depicted in Fig. 2.

## III. DESCRIPTION OF THE RAY-TRACING SIMULATIONS

### A. Ray-tracing description

The 3D ray-tracing tool used as simulator was programmed in MATLAB by the authors and it has been validated in several indoor environments [19]. It is based on image theory, and it includes both specular and diffuse scattering components. The accuracy of a ray-tracing simulation depends mainly on the following key aspects: the accuracy of the geometrical model of the environment, a wide variety of propagation mechanisms, a high enough order of the propagation mechanisms, the appropriate selection of the elements' electromagnetic properties, and the accuracy of the antenna patterns.

A geometrical model composed of rectangles and circular cylinders was developed to represent the metro convoy. The model is shown in Fig. 4 and it includes all main elements: the walls, the doors, the windows of both walls and doors, the handholds, the junctions that flank the doors, and the seats. When the simulation of a particular Tx-Rx combination is performed, a simplified

model of the own Rx subsystem is added to the geometrical model; the Rx subsystem attenuates some rays and must be included to improve the accuracy; the model is composed of the VNA and the computer, represented with a cube, the XY positioning system represented with a rectangle, and the receiver antenna represented with a small cube, as seen in Fig. 4. All convoy elements are represented using rectangles except

the handholds which have a curved shape as seen in Fig. 1. Thus, the handholds are modeled as circular cylinders; the radius of all cylinders were set to 2 cm. When a reflected ray is created from a handhold the appropriate formulation for curved objects is applied. The total number of rectangles is 1769, a large number needed to properly represent the environment.

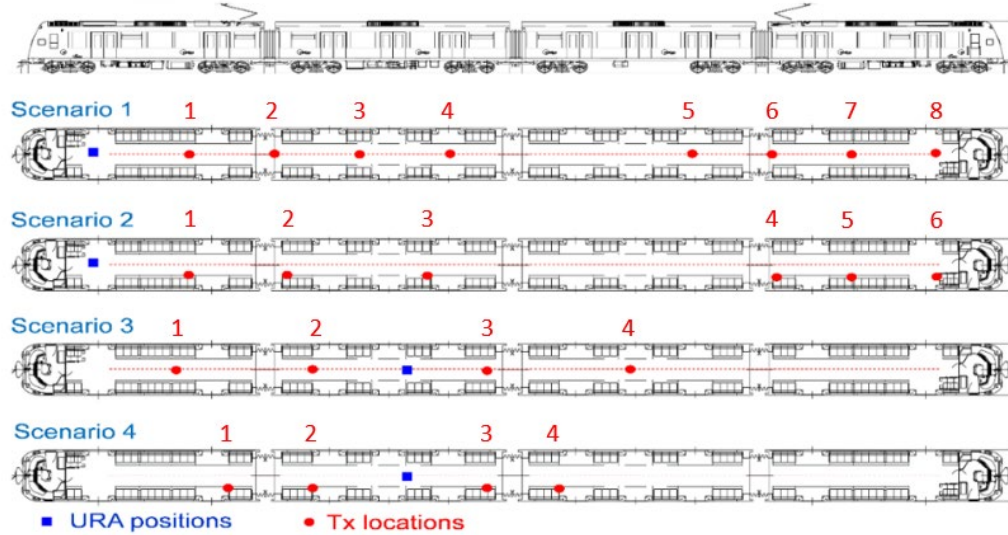


Fig. 2. Map of the measurements. The URA is the Rx and the Tx positions are numbered.

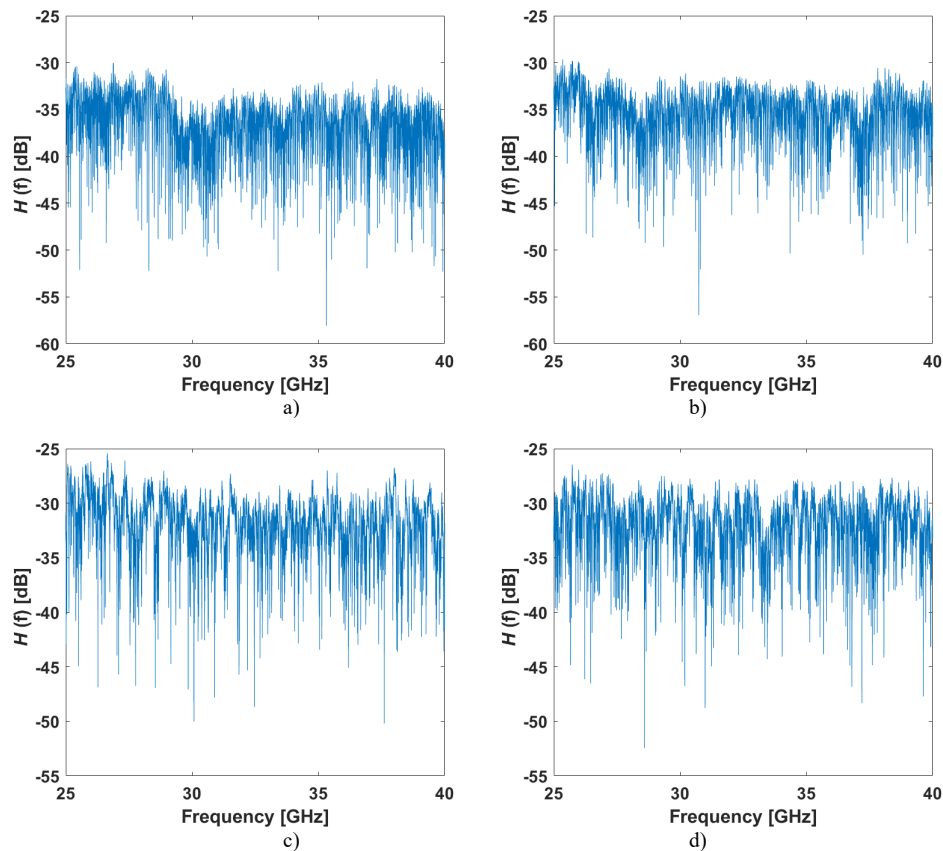


Fig. 3. Measured frequency transfer function  $H(f)$  at the central element of the virtual URA of position 4 of a) scenario 1, b) position 3 of scenario 2, c) position 3 of scenario 3, and d) position 3 of scenario 4.

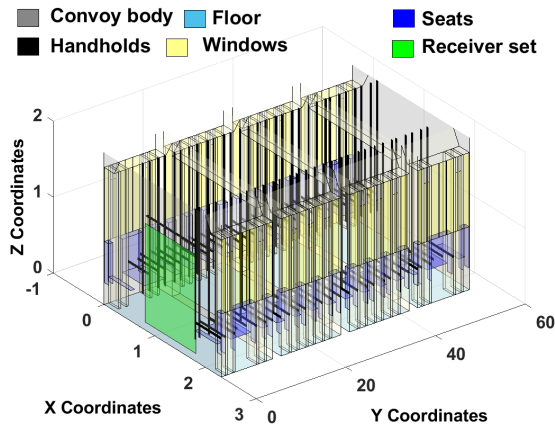


Fig. 4 Geometric model of the metro convoy and the receiver subsystem.

Down below the simulated propagation mechanisms are described and the abbreviation used in this paper is introduced:

- DR: direct ray. The Tx-Rx LoS ray.
- R1, R2 and R3: first, second and third-order reflections on flat surfaces, respectively.
- D: single diffractions on straight wedges.
- SC: diffuse scattering. To simulate these components, we have used the Lambertian and directive models described in [20]. These models are derived from the Effective Roughness model. Both models have one parameter, named as  $S$ , which controls the percentage of the energy scattered in all directions. The directive model has an additional parameter, named as  $\alpha$ , which controls how the scattering lobe is steered towards the direction of the specular reflection. The geometrical model is sampled to produce a set of points that produce diffuse scattering waves; the distance between two consecutive points as set to  $4\lambda$ , where  $\lambda$  was computed at the central frequency of the whole band.
- R1D: first-order reflections and a subsequent single diffraction. These components firstly undergo a reflection on a flat surface and subsequently the wave is diffracted on a straight edge.
- R2D: second-order reflections and a subsequent single diffraction. These components firstly undergo two consecutive reflections on flat surfaces and subsequently the wave is diffracted on a straight edge. This mechanism consumes large amounts of computer resources. The simulation was infeasible using the complete geometrical model. Several tests showed that the main reflection components corresponded to the back-and-forth reflections on the ends of the convoy; thus, a simplified version of the geometrical model, including only the ends of the convoy and the sidewalls and junctions between

wagons where the diffraction takes place, was used to simulate these replicas.

- DR1: diffraction and a subsequent first-order reflection. These components firstly undergo a diffraction on a straight edge and subsequently the wave undergoes a reflection on a flat surface.
- DR2: diffraction and a subsequent second-order reflection. These components firstly undergo a diffraction on a straight edge and subsequently the wave undergoes two consecutive reflections on a flat surface. Just like the R2D mechanism a simplified model was used to simulate these rays.
- R1H: first-order reflections on handholds. These components are single reflections on the curved shape handholds. An appropriate formulation described in [21] was used to simulate this propagation mechanism. In this mechanism only one ray is considered; this ray corresponds to the minimum Tx-handhold-Rx distance and can be easily found.

The maximum propagation mechanism order is three (R3, R2D, and DR2). As we will show in the following sub-section, this order is enough to recreate in the simulation most of the main rays present in the measurements.

The electromagnetic properties of the materials in the environment must be correctly assigned. Although several studies have estimated the electromagnetic properties of common materials for low mm-Wave bands [22], many materials have not been characterized yet. In this way, we have used the general equations for materials found in the ITU Recommendation P.1238-7 [23]; these equations are valid between 1–100 GHz, and they provide a good approximation of the electromagnetic properties. A tuning step was applied to find a proper value of the scattering parameters of the environment. The flowchart of the general procedure used to tune the electromagnetic properties is shown in Fig. 5. The used cost function is the mean of the absolute value of the difference between the measured and simulated PDP as defined in [24]:

$$\varepsilon = \frac{1}{J} \sum_{j=1}^J |PDP_{meas}(j) - PDP_{sim}(j)|, \quad (1)$$

where  $PDP_{meas}$  is the measured PDP,  $PDP_{sim}$  is the simulated PDP including all components, and the  $j$  indices correspond to those values of the measured PDP above a threshold of 30 dB. The cost function was evaluated by changing  $S$  from 0.3 to 0.9 in steps of 0.1; for the directive model,  $\alpha$  was set to 1. The tuning step follows a brute force search procedure, this way, the best value, which minimizes the cost function, is selected from the whole set of values.

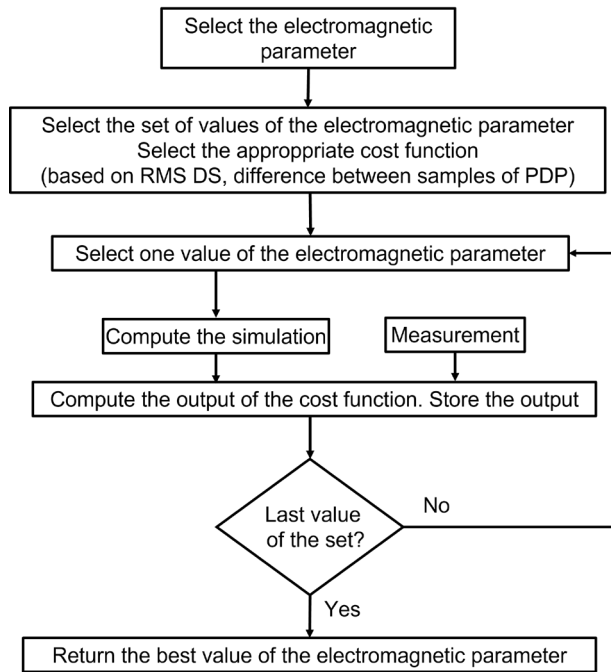


Fig. 5. Flowchart of the tuning procedure of the electromagnetic properties.

As seen in Fig. 6 the directive model yields smaller values of the cost function than the Lambertian model in

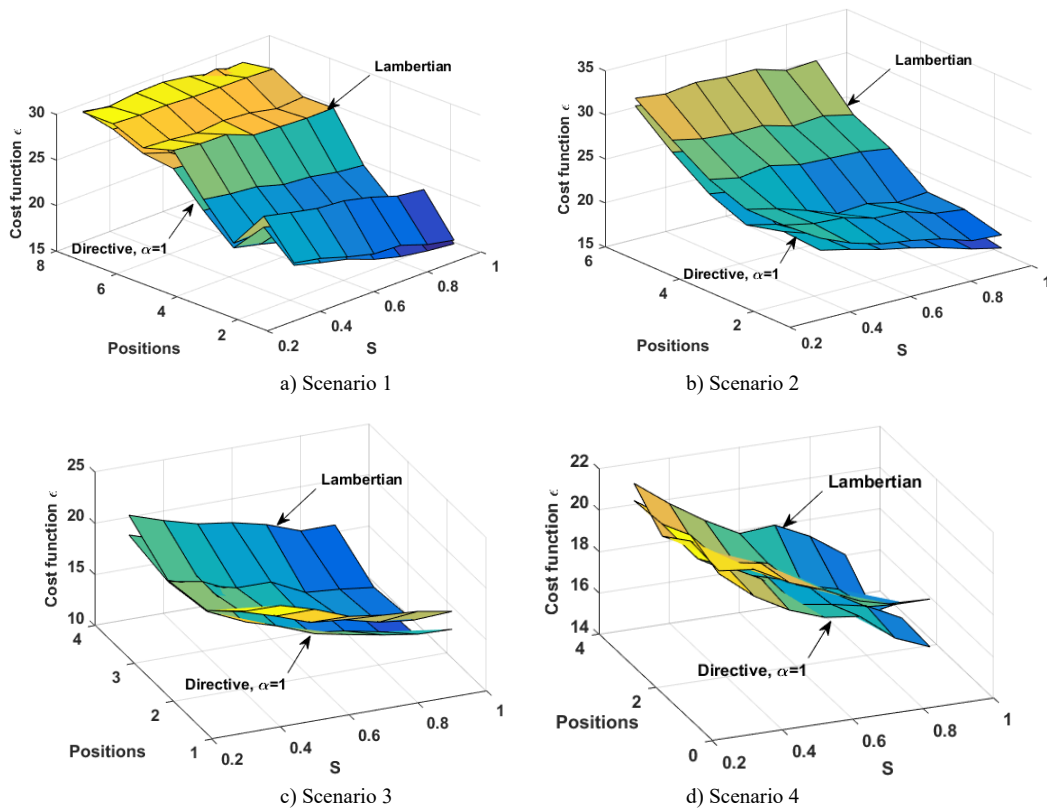


Fig. 6. Value of the cost function in dB defined in (1) in the diffuse scattering parameter  $S$  optimization problem for all positions of the scenarios (a) Scenario 1, b) Scenario 2, c) Scenario 3, and d) Scenario 4). The  $S$  parameter ranges from 0.3 to 0.9.

all scenarios. The optimal values of  $S$  ranged from 0.7 to 0.90 in the different positions and scenarios; the mean of the of the optimal values was 0.85 and it was selected as the final value of  $S$  in all materials of the environment.

All values of the real part of the permittivity and conductivity are shown in Table I. The permittivity and conductivity for the glass, present in the windows, was determined using [23]. The floor is made of stratified rubber, since this material is not present in [23] we have used the value available in [25] corresponding to typical plastic materials similar to stratified rubber. Although good results were obtained considering the convoy body as a metal, the tuning phase shown in Fig. 5, using the RMS DS as cost function, was applied to the permittivity and conductivity of the mentioned element to improve the accuracy; the final value has a relatively high real value of permittivity and high conductivity; using the tuned values the accuracy of the RMS DS, in simulations at one frequency applying a threshold of 30 dB, was 67.7% whereas using the metal material the accuracy was 59.3%.

The seats are made of resin-molded, to the best of the authors' knowledge the permittivity of this material is not available in the literature for the analyzed band; nevertheless, we have used the value of plastic ABS, obtained from [25], such material is usually employed in seats, and it is similar to the material used in the seats of the scenario. All remaining elements are composed of metallic materials as stainless steel and aluminum. As explained previously, the Rx subsystem model is included in the geometrical model, and a tuning phase, based on the procedure shown in Fig. 5, was applied to find a proper attenuation, which was set to 5 dB/m.

TABLE I

ELECTROMAGNETIC PROPERTIES OF THE ELEMENTS FOR THE CENTRAL FREQUENCY OF THE BAND.

Element	Material	$\epsilon_r$	$\sigma$ [S/m]
Windows	Glass	6.3	0.3
Floor	Plastic	3.6	0.5
Convoy body	Plastic	10.0	30.0
Seats	ABS	2.5	2.0
Convoy ends	Metal	—	$4 \cdot 10^7$
Ceiling	Metal	—	$4 \cdot 10^7$
Handholds	Metal	—	$4 \cdot 10^7$
Doors	Metal	—	$4 \cdot 10^7$

As explained in sub-section II.B, the channel frequency transfer measurement includes the antennas effect. It is cumbersome to remove the antenna gains from the measurements to show only the propagation effects when a comparison between simulations and measurements is desired. Therefore, the antenna patterns are usually incorporated into the simulations. To improve the accuracy, the antenna patterns were measured in an anechoic chamber at different frequencies between 25–40 GHz. In Fig. 7 the 3D antenna patterns are depicted for two frequencies.

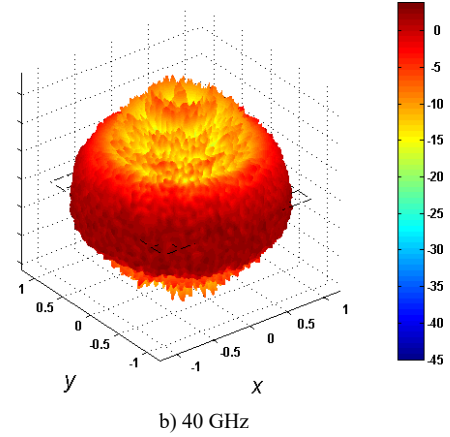
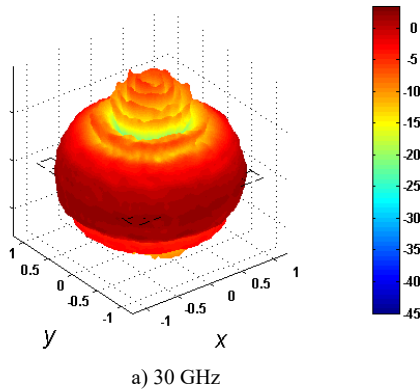


Fig. 7. Measured antenna pattern in dB for two frequencies: a) 30 GHz and b) 40GHz

### B. Simulations accuracy analysis

Three parameters have been used to analyze the accuracy of the ray-tracing simulator: the RMS DS, the mean delay, and the path loss magnitude. The path loss includes the antennas gain and it is usually represented as PL (this magnitude is named as transmission loss by the ITU and it is described as L). All of them can be extracted from the PDP, which can be estimated averaging the channel impulse response (CIR) over the 49 positions of the URA:

$$P(\tau) = \overline{|h(\tau)|^2}, \quad (2)$$

where  $h(\tau)$  is the CIR. Each CIR is obtained by applying the inverse Fourier transform to the  $H(f)$  function. The Hanning window is applied in the frequency domain to obtain a better representation of the replicas in the time domain. Once the PDP is estimated, the RMS DS is defined as:

$$\tau_{rms}(s) = \sqrt{\frac{\sum_k P(\tau_k) \tau_k^2}{\sum_k P(\tau_k)} - \left( \frac{\sum_k P(\tau_k) \tau_k}{\sum_k P(\tau_k)} \right)^2}, \quad (3)$$

where  $\tau_k$  is the  $k$ -th delay and  $P(\tau_k)$  is the linear value of the PDP at  $\tau_k$ . The mean delay is defined as:

$$\bar{\tau}(s) = \frac{\sum_k P(\tau_k) \tau_k}{\sum_k P(\tau_k)}. \quad (4)$$

Finally, the PL can be estimated in the time domain using the PDP as:

$$PL \text{ (dB)} = -10 \log_{10} \left( \sum_k P(\tau_k) \right). \quad (5)$$

The delay parameters are calculated by applying a threshold to select the significant multipath components and to remove the noise. In Fig. 8 the measured and simulated PDP are shown for position 2 of scenario 2; the 25 dB, 30 dB and 35 dB thresholds are also shown. In

Fig. 9 the measured and simulated RMS DS values as well as the achieved accuracy (difference in % between the measured and simulated value) are shown for the mentioned position. As seen in Fig. 8 at 316 ns (equivalent to 94.8 m) there is a significant power multipath component; when a threshold of 25 dB is applied, the simulated component is selected, whereas the measured component is not included in the RMS DS estimation; this fact produces a low value of accuracy of 54 %, as seen in Fig. 9. Nevertheless, when the threshold is 30 dB, both measured and simulated components at 316 ns are selected, increasing the accuracy to a value equal to 81.5%. Additionally, when the threshold is 30 dB a new measured component at 329.5 ns (98.85 m) is included, whereas the simulated one is not yet selected. When the threshold rises to 35 dB, the simulated component at 329.5 ns is selected and the accuracy is again improved up to 99.2 %.

Therefore, in this kind of rich multipath environment, where components with significant power and considerable delays exist, even though the main components are simulated as seen in Fig. 8, a slight difference in the threshold can lead to large differences in the accuracy. In this way, instead of using a fixed threshold to analyze the accuracy of the simulations, we have used a set of thresholds between 20 dB and 40 dB; consequently, the average of the accuracies obtained with the set of thresholds has been used to compare measurements and simulations. For example, for position 2 of scenario 2 the average of the accuracy of the RMS DS is 81 % as shown in Fig. 9. To complete the analysis of the performance of the simulations the standard deviation of the accuracies has also been computed. The PL is computed without applying any threshold since it is, by definition, the sum of all values of the PDP as seen in (5); thus, neither average nor standard deviation is shown for this parameter. To conclude the analysis of the accuracy, the path loss model parameters have also been calculated using the measured and simulated *PL* values.

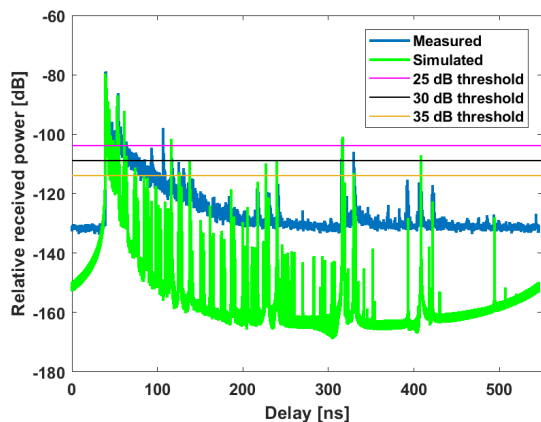


Fig. 8. Measured and simulated PDPs of position 2 of scenario 2. Three different thresholds are depicted.

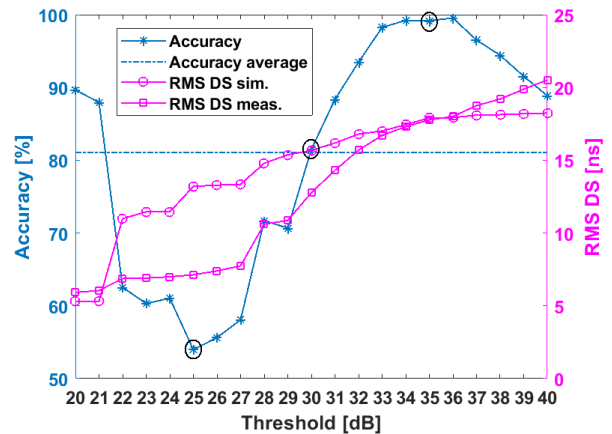


Fig. 9. Measured RMS DS, simulated RMS DS, accuracy, and average of the accuracy for position 2 of scenario 2.

The parameters values and the accuracy for all positions of scenario 1 are shown in Table II. In this scenario the Rx is close to the cabin and the Tx imitates a standing passenger. The RMS DS accuracy is excellent in all positions except for position number 8; in this case there is a three order reflection with a considerable delay which has a wrong value of simulated power. In the rest of positions, the measured and simulated RMS DS average values are similar. The standard deviation of the measured RMS DS is larger than the simulated one. The mean delay accuracy is also good; all values are above 86 %. As in the RMS DS, the standard deviation of the measurements is larger than the values obtained in the simulations. The difference between the measured and simulated PL is small for all positions except for the position 8 where the difference is larger than 5 dB.

Table III shows the results for all positions of scenario 3. As seen in Fig. 2, in this scenario the Rx is in the middle of the convoy and the Tx imitates a standing passenger as in scenario 1. The RMS DS accuracy achieves larger values, above 70 % for all Tx positions; the values of the measured and simulated RMS DS average are very similar for positions 2 and 3 (located close to the Rx), whereas more significant differences are found for positions 1 and 4. The accuracy of the mean delay is high, all values are above 88 %. Again, the standard deviation of the measurements is larger than the standard deviation of the simulations. Finally, the PL differences are below 3 dB, a relatively good result.

The Table IV shows the results for all positions of scenario 2. In this scenario, the Rx is located close to the cabin and the Tx imitates a seated passenger, as seen in Fig. 2. The accuracy of the RMS DS reaches high values in positions {1-3, 5} and lower values in positions {4, 6}. The measured and simulated RMS DS average values are logically similar for positions with higher accuracy and show larger differences for positions 4 and 6. The mean delay accuracy is very high as in the previous cases. Again, the standard deviation of the measurements is larger than the standard deviation obtained in the simulations. The PL differences show values below 4 dB,

ranging from the lowest value of 0.53 dB to the highest value of 3.90 dB.

Table V shows the results for all positions of scenario 4. In this scenario, the Rx is in the middle of the convoy and the Tx imitates a seated passenger as in the previous case. In the RMS DS, two positions {2, 3} achieve large values of accuracy whereas the other two positions achieve accuracies of 67 %. As in scenario 3 the measured and simulated RMS DS average values are more similar

in those positions where the Tx is near the Rx (2 and 3) than in those positions located farther (1 and 4). The mean delay accuracy is high; values above 89 % are obtained for all positions. The standard deviation of the measured values is in general higher than the standard deviation found in the simulations. The PL differences are below 3 dB.

TABLE II

RMS DS, MEAN VALUE OF DELAY AND PATH LOSS ACCURACY FOR SCENARIO 1. THE THRESHOLD VARIES FROM 20 DB TO 40 DB. MEAS. ARE THE MEASURED VALUES AND SIM. THE SIMULATED VALUES.

Position	Type	RMS DS average (ns)	RMS DS std. dev. (ns)	Average Accuracy (%)	Mean delay average (ns)	Mean delay std. dev. (ns)	Average Accuracy (%)	Path loss (dB)	Path loss difference (dB)
1	Meas.	15.06	5.14	85	25.11	1.33	86	65.34	0.64
	Sim.	12.72	3.84		21.52	0.41		64.70	
2	Meas.	22.37	5.96	79	40.67	2.01	90	70.23	1.83
	Sim.	19.90	1.03		36.52	0.26		68.40	
3	Meas.	25.17	3.48	94	55.90	1.75	95	72.30	2.25
	Sim.	23.88	2.20		52.86	0.45		70.05	
4	Meas.	34.83	5.91	90	82.51	3.07	91	76.21	1.85
	Sim.	37.67	2.32		74.85	0.80		74.36	
5	Meas.	42.02	4.31	91	138.91	2.69	98	78.29	1.50
	Sim.	45.23	1.08		135.40	0.46		79.79	
6	Meas.	46.77	5.07	80	169.46	3.29	88	81.66	1.85
	Sim.	37.06	1.72		148.62	0.61		79.81	
7	Meas.	31.80	3.23	92	182.15	1.89	90	80.71	0.30
	Sim.	29.33	1.83		163.82	0.42		81.01	
8	Meas.	16.83	2.60	52	188.70	1.09	94	78.02	5.64
	Sim.	32.39	2.09		177.48	0.52		83.66	

TABLE III

RMS DS, MEAN VALUE OF DELAY AND PATH LOSS ACCURACY FOR SCENARIO 3. THE THRESHOLD VARIES FROM 20 DB TO 40 DB. MEAS. ARE THE MEASURED VALUES AND SIM. THE SIMULATED VALUES.

Position	Type	RMS DS average (ns)	RMS DS std. dev. (ns)	Average Accuracy (%)	Mean delay average (ns)	Mean delay std. dev. (ns)	Average Accuracy (%)	Path loss (dB)	Path loss difference (dB)
1	Meas.	30.36	4.12	80	59.21	3.29	96	74.61	0.75
	Sim.	37.82	088		59.20	0.48		73.86	
2	Meas.	12.27	5.61	74	21.20	1.90	94	67.71	2.11
	Sim.	15.62	2.85		20.53	0.59		65.60	
3	Meas.	13.57	6.52	75	21.32	2.14	93	67.17	2.64
	Sim.	12.74	3.48		20.00	0.61		64.53	
4	Meas.	37.08	2.02	71	61.21	2.27	88	75.38	2.64
	Sim.	26.50	1.60		53.66	0.59		72.74	

TABLE IV

RMS DS, MEAN VALUE OF DELAY AND PATH LOSS ACCURACY FOR SCENARIO 2. THE THRESHOLD VARIES FROM 20 DB TO 40 DB. MEAS. ARE THE MEASURED VALUES AND SIM. THE SIMULATED VALUES.

Position	Type	RMS DS average (ns)	RMS DS std. dev. (ns)	Average Accuracy (%)	Mean delay average (ns)	Mean delay std. dev. (ns)	Average Accuracy (%)	Path loss (dB)	Path loss difference (dB)
1	Meas.	8.33	2.33	92	22.91	1.84	91	63.94	3.38
	Sim.	8.13	2.45		20.74	0.30		67.32	
2	Meas.	12.73	5.37	81	44.85	1.78	97	70.43	1.27
	Sim.	14.53	3.91		43.30	0.50		71.70	
3	Meas.	34.54	2.96	90	77.58	1.94	95	73.60	2.12
	Sim.	30.75	1.92		73.93	0.55		75.72	
4	Meas.	42.24	4.01	61	160.13	3.08	86	81.26	0.53
	Sim.	25.33	2.04		138.10	0.40		81.79	
5	Meas.	21.05	5.45	78	162.74	1.99	97	80.00	2.16
	Sim.	26.31	2.08		157.03	0.46		82.16	
6	Meas.	18.48	5.91	54	177.46	2.30	98	80.87	3.90
	Sim.	34.27	1.27		174.39	0.50		84.77	

TABLE V

RMS DS, MEAN VALUE OF DELAY AND PATH LOSS ACCURACY FOR SCENARIO 4. THE THRESHOLD VARIES FROM 20 dB TO 40 dB. MEAS. ARE THE MEASURED VALUES AND SIM. THE SIMULATED VALUES.

Position	Type	RMS DS average (ns)	RMS DS std. dev. (ns)	Average Accuracy (%)	Mean delay average (ns)	Mean delay std. dev. (ns)	Average Accuracy (%)	Path loss (dB)	Path loss difference (dB)
1	Meas.	26.65	5.00	67	41.32	2.52	89	69.87	0.31
	Sim.	17.72	2.72		36.73	0.53		69.56	
2	Meas.	15.52	4.99	89	23.31	2.13	92	66.38	1.82
	Sim.	13.92	3.35		21.48	0.71		68.20	
3	Meas.	15.31	3.84	84	23.68	1.98	89	66.99	2.19
	Sim.	13.07	3.80		20.90	0.74		69.18	
4	Meas.	24.43	3.47	67	41.03	2.22	91	71.37	1.18
	Sim.	16.24	1.57		37.32	0.40		70.19	

Finally, Table VI shows the comparison between the measured and simulated path loss model parameters for all scenarios. We have used the *floating-intercept* (FI) path loss model defined as [5]:

$$PL^{FI}(d) = \beta + 10\alpha \log_{10}(d), \quad (6)$$

where  $\beta$  is the floating-intercept parameter (offset term) and  $\alpha$  is the path loss exponent.

The accuracy is good for all scenarios except for scenario 4; in this scenario only four positions are considered and the larger errors at positions 2 and 3 have a relevant impact on the path loss exponent. The results shown in Table VI agree with the ones found in [4] where the path loss exponent was also below the free space one ( $\alpha=2$ ). This fact is due to the elongated structure of the environment and the presence of many metallic objects (waveguide effect).

TABLE VI  
PATH LOSS MODEL PARAMETERS

		$\beta$ (dB)	$\alpha$
Scenario 1	Meas.	55.27	1.50
	Sim.	50.05	1.88
Scenario 2	Meas.	51.10	1.78
	Sim.	53.86	1.74
Scenario 3	Meas.	55.34	1.70
	Sim.	51.89	1.85
Scenario 4	Meas.	56.82	1.38
	Sim.	65.71	0.42

We can conclude that the accuracy of the analyzed parameters is significant in general. The confined structure and the presence of many metallic objects makes the intra-wagon a rich multipath environment; using a maximum order of three in the simulated rays was enough to achieve the needed accuracy. Values above 70 % are obtained for many positions and the differences between the measured and simulated PL are small. However, the accuracy is larger for scenarios 1 and 3 than for scenarios 2 and 4. Therefore, the simulation of positions that

imitate a seated passenger is more troublesome than the simulation of the standing passengers' positions. This fact is due to the presence of handholds close to the Tx in scenarios 2 and 4; in these cases, a small error in the location of the Tx in the geometrical model can lead to significant errors in the simulations, since rays blocked by a handhold can be incorrectly included in the simulation. The standard deviation of the measured RMS DS and mean delay values are in general higher than the simulated ones; this fact is due to the absence of some components in the simulations. For example, the measured components with delays around 100 ns in Fig. 8 are not present in the simulations.

The measured RMS DS in this work is much larger than the values obtained in other measurements found in the literature. Thus, in [15] the RMS DS measured in a high-speed train was 0.92–3.24 ns at 60 GHz and 1.15 ns–2.57 ns at 300 GHz; in [16] the RMS DS in a metro train at the 26.5–40 GHz band was in the range 0.36–0.76 ns. In [15] some of the Tx-Rx configurations were similar to the ones shown in scenarios 1 and 3; however, the higher bands are much less time dispersive than the lower ones and therefore lower RMS DS are expected in low mm-Wave bands. In [16] the Rx were close to the sidewalls and the main rays had small delays; in our Tx-Rx configurations and metro train, large delays rays are present, even in the case of the seated passenger. Therefore, an analysis about the relevant rays in the environment for the selected band is required.

#### IV. SIMULATIONS RESULTS

The ray-tracing tool provides a complete description of the paths of the components. Thus, we can get insight into the wireless channel, analyzing which the main components and propagation mechanisms are present, and obtaining the angular spread, which is complex to extract accurately from the measurements [19].

##### A. Analysis of the propagation mechanisms

The paths are calculated at the central frequency of the whole band and at one Rx of the URA. A threshold of 20 dB has been

applied in all cases to show only the main components, and the direct ray is not depicted since it is always a main component in all positions. Each case shows interesting characteristics of the propagation mechanisms in the analyzed environment. The following colors have been used to distinguish one kind of propagation mechanism from another:

- Reflections (R1, R2, and R3): magenta.
- Diffractions (D): green.
- Reflections and diffractions and vice versa (R1D, R2D, DR1, and DR2): brown.
- Reflections on handholds (R1H): orange.

The remaining propagation mechanisms have powers below the chosen threshold.

Firstly, position number 1 of scenario 1 is analyzed; in this position the Tx is close to the Rx and imitates a standing passenger. In Fig. 10 the main components are depicted. Most of the components have an elevation angle close to  $90^\circ$  and correspond to reflections in the elements of the walls close to the Tx and Rx; the rest of rays having powers above the threshold come from the ceiling. The obtained CIR is compared with the measured PDP in Fig. 11, where each relevant ray is depicted using the assigned color and the remaining components are plotted in black. All relevant rays have small delays close to the direct ray. As the Tx-Rx distance increases the back-and-forth reflections on the ends of the convoy become more relevant and exceed the threshold. Moreover, new rays as diffracted rays and reflected and diffracted rays appear.

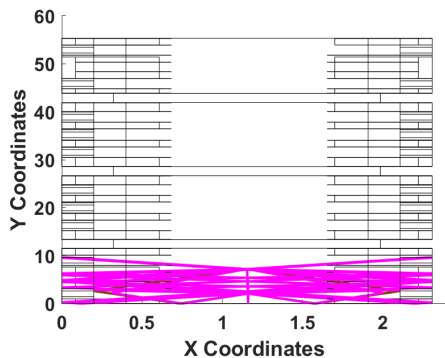


Fig. 10. Main rays for position 1 of scenario 1.

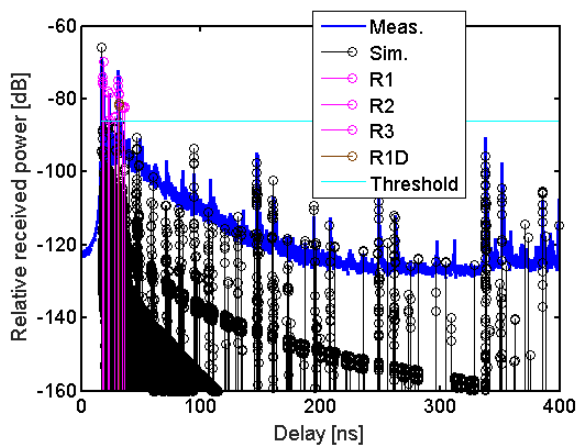


Fig. 11. Simulated CIR of position 1 of scenario 1 and measured PDP. The threshold of 20 dB is depicted in cyan.

In scenario 3 the URA Rx is in the middle of the convoy and the Tx imitates a standing passenger as in scenario 1. The rays with powers above the threshold of 20 dB of position 4 are shown in Fig. 12. There are reflected rays, diffracted rays, and reflected and diffracted rays. The main rays come from the walls' elements of the convoy and from the first-order reflections on the ends. In Fig. 13 the simulated CIR and the measured PDP are shown. Most of the rays have delays close to the delay of the direct ray although four rays with larger delays have significant powers above the threshold. Firstly, a second-order reflection on the ceiling and a reflected and diffracted ray on the ceiling, having both delays around 91.5 ns (27.5 m). Secondly, the first order reflections on the ends of the convoy with delays of 180 ns (54 m) and 188 ns (56.4 m).

We can conclude that, when the passenger is standing and close to the access point, the main rays come from the elements present in the walls; moreover, when the passenger is not close to the access point the reflections on the ends of the convoy are relevant and contribute largely to the delay spread, since these components have relatively large powers and very substantial delays. The rays coming from the floor and ceiling exceed the threshold, but they are less relevant than the rays with elevation angles close to  $90^\circ$ , coming from the walls and from the ends of the convoy.

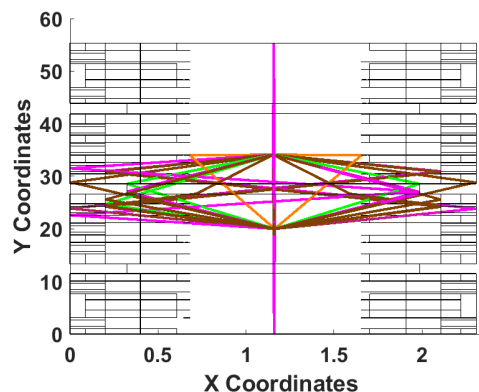


Fig. 12. Main rays for position 4 of scenario 3.

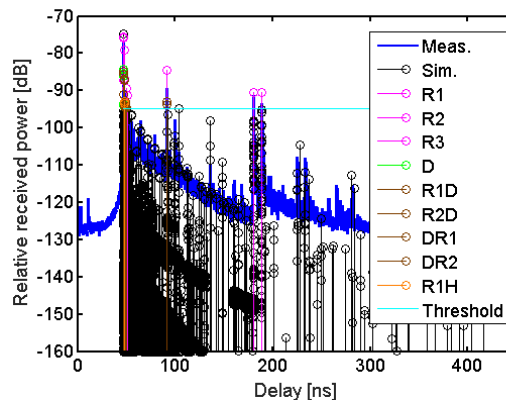


Fig. 13. Simulated CIR of position 4 of scenario 3 and measured PDP. The threshold of 20 dB is depicted in cyan.

The contribution of each propagation mechanism to the total power can be estimated analytically. In Table VII and Table VIII, the percentage of the simulated power of each propagation mechanism, without applying any threshold, is shown for all positions of scenario 1 and scenario 3, respectively. Since all

positions are in a LoS situation the direct ray is always a significant propagation mechanism. Reflections, produced by the elements present in the walls, the walls, the floor and ceiling, and the metallic ends of the convoy, are the second largest power propagation mechanism. The diffracted rays and the rays produced by combinations of reflections and diffractions are also relevant in certain transmitter locations; the most important rays of this group of components come from the junctions of the walls, where the elevation angles are close to  $90^\circ$  and the receiver position is close to the reflection shadow boundary (RSB), where the diffraction coefficient exhibits a maximum [21]. As the transmitter moves to another location the receiver position moves away from the RSB and the diffracted rays become less relevant.

In scenarios 2 and 4 the Tx imitates a seated passenger. In Fig. 14 the rays above the threshold of 20 dB are shown for position 3 of scenario 2. As seen in Fig. 15 there are four groups of significant components. The rays of the first group have delays close to the delay of the direct ray. The rays of the second have delays around 81 ns (24.3 m). These first two groups correspond to reflections, diffractions and the combination of reflections and diffractions; all these rays come from the elements present in the convoy walls and from the ceiling and floor. The rays of the third group have delays around 288 ns (86.4 m). Although the simulated rays of the fourth group are below the threshold the measured ones are above the threshold, this way it is interesting to identify these rays with delays around 301 ns (90.3 m); these last two groups have larger delays than the first two groups and are composed of reflections where the ends of the convoy are involved.

TABLE VII

PERCENTAGE OF POWER OF EACH SIMULATED PROPAGATION MECHANISM.  
SCENARIO I.

	P1	P2	P3	P4	P5	P6	P7	P8
DR	36.48	19.16	18.92	17.09	18.64	15.95	13.84	22.43
R1	32.70	56.14	29.68	30.51	11.75	8.55	19.15	12.96
R2	11.73	10.52	10.44	4.27	7.26	24.06	12.24	3.64
R3	5.30	4.27	9.36	9.75	3.68	4.37	4.98	4.12
D	0.18	0.81	9.22	7.50	23.17	16.32	16.73	23.93
SC	8.66	3.03	2.65	2.27	2.05	1.70	1.44	2.66
R1D	0.47	0.41	1.97	6.64	11.66	11.84	11.42	10.59
R2D	0.12	0.17	0.17	0.27	0.38	0.41	0.44	0.54
DR1	2.84	4.33	16.29	18.40	19.38	15.50	17.74	16.51
DR2	0.04	0.05	0.44	2.16	0.84	0.48	1.24	1.81
RH	1.49	1.11	0.86	1.15	1.19	0.81	0.78	0.81

TABLE VIII

PERCENTAGE OF POWER OF EACH SIMULATED PROPAGATION MECHANISM.  
SCENARIO 3.

	P1	P2	P3	P4
DR	27.08	46.77	32.44	20.73
R1	35.33	24.70	36.11	45.43
R2	5.53	2.39	5.31	6.14
R3	2.32	3.36	3.54	2.19
D	9.49	7.48	11.18	7.25
SC	2.18	6.17	4.86	2.28
R1D	5.69	4.73	2.31	3.20
R2D	1.34	0.11	0.11	0.70
DR1	8.84	2.26	2.62	9.91
DR2	0.84	0.10	0.05	0.70
RH	1.37	1.94	1.46	1.48

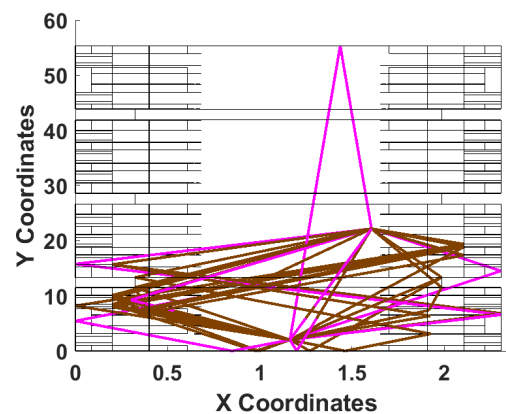


Fig. 14. Main rays for position 3 of scenario 2.

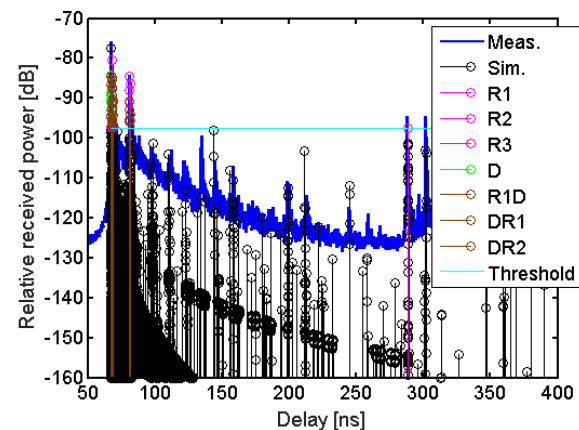


Fig. 15. Simulated CIR of position 3 of scenario 2 and measured PDP. The threshold of 20 dB is depicted in cyan.

In Fig. 16 the rays above the threshold of 20 dB are shown for position 4 of scenario 4. Four groups of rays are identified in Fig. 17. The first group, as in the previous case, is composed of rays coming from the walls, from their elements, the ceiling, and the floor; these rays have delays close to the delay of the direct ray. The other three groups have larger delays and correspond to first and second order reflections on the ends of the convoy. The simulated rays of the last group are below the threshold whereas the measured ones are above the threshold.

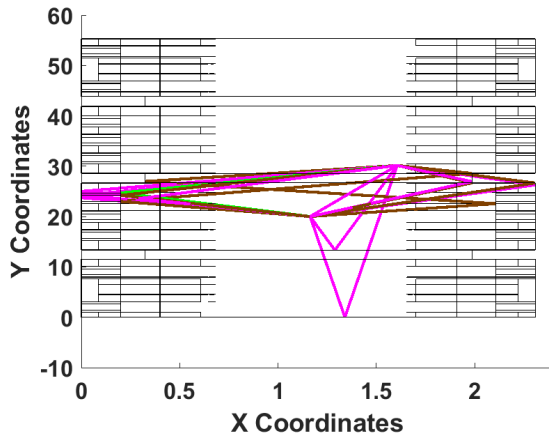


Fig. 16. Main rays for position 4 of scenario 4.

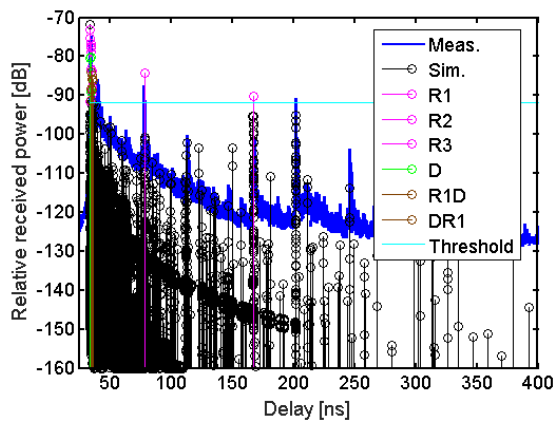


Fig. 17. Simulated CIR of position 4 of scenario 4 and measured PDP. The threshold of 20 dB is depicted in cyan.

In Table IX and Table X, the percentage of the simulated power of each propagation mechanism is shown for all positions of scenario 2 and scenario 4, respectively. As in scenarios 1 and 3, the direct ray and the reflections are the largest power propagation mechanism. The diffracted rays and the rays produced by combinations of reflections and diffractions are relevant in some positions, when the receiver is close to the RSB [21].

TABLE IX

PERCENTAGE OF POWER OF EACH SIMULATED PROPAGATION MECHANISM. SCENARIO 2.

	P1	P2	P3	P4	P5	P6
DR	33.86	24.62	21.58	22.83	25.26	26.02
R1	34.37	40.18	14.57	23.94	14.26	16.10
R2	14.67	13.09	8.71	10.05	11.70	12.22
R3	2.96	6.05	3.70	8.92	6.24	5.50
D	0.20	1.94	11.78	9.51	14.30	9.59
SC	10.72	3.44	2.99	2.77	2.94	3.46
R1D	1.02	0.63	6.79	8.27	15.87	9.47
R2D	0.05	0.14	0.19	0.64	1.14	1.89
DR1	0.79	9.15	24.97	9.82	7.12	13.21
DR2	0.01	0.04	4.03	2.37	0.53	1.97
RH	1.35	0.72	0.69	0.88	0.64	0.57

TABLE X

PERCENTAGE OF POWER OF EACH SIMULATED PROPAGATION MECHANISM. SCENARIO 4.

	P1	P2	P3	P4
DR	24.40	42.67	43.62	23.00
R1	38.93	27.19	25.50	40.94
R2	15.14	9.38	9.45	15.57
R3	1.53	6.89	5.21	1.33
D	7.20	0.94	0.96	7.57
SC	2.53	8.33	9.12	2.51
R1D	2.68	1.11	0.86	3.01
R2D	0.41	0.12	0.10	0.24
DR1	5.98	2.09	3.80	5.01
DR2	0.19	0.02	0.01	0.19
RH	1.02	1.26	1.36	0.62

We can conclude that the type of relevant components found when the Tx emulates a seated passenger are similar to those found in the standing passenger case. The main rays come from the walls, ceiling and floor, having delays close to the direct ray, and from reflections on the ends of the convoy, having larger delays. However, there are some significant differences. When the passenger is standing most of the rays coming from the walls show elevation angles around 90°, whereas a somewhat wider spread in elevation angles exists when three conditions hold: the passenger is seated, the Tx-Rx distance is not small, and the Rx is in the middle of the convoy. The single and multiple reflections on the ends of the convoy produce large delays in both situations; nevertheless, when the passenger is standing the powers of such components are larger than in the seated case; this fact is due to the antenna pattern which has a maximum gain when the elevation angle is close to 90°. In [16] the handholds, junctions present in the walls and the main boy of the train were identified as the main contributors to the multipath components. We have found that, in the presented Tx-Rx locations, the metallic ends of the convoy are of great importance; moreover, we have found that the reflected components coming from the handholds are not negligible but play a secondary role in the multipath propagation; in [16] each Rx was almost surrounded by handholds (poles) and therefore they were more relevant.

### B. Angular spread

The angles of arrival and departure are obtained from the ray-tracing simulations. The reference shown in Fig. 18 has been used to calculate the azimuth angles; the azimuth angles range between 0° and 180° and 0° and -180°, depending on the direction of the ray; the elevation angles range between 0° and 180°.

The AS in azimuth and elevation for direction of arrival and departure angles can be calculated using [19]:

$$AS(^{\circ}) = \sqrt{\frac{\sum_k P(\tau_k) \alpha_k^2}{\sum_k P(\tau_k)} - \left( \frac{\sum_k P(\tau_k) \alpha_k}{\sum_k P(\tau_k)} \right)^2}, \quad (7)$$

where  $\alpha_k$  is equal to  $\theta_{TX}$  (°),  $\theta_{RX}$  (°),  $\varphi_{TX}$  (°), and  $\varphi_{RX}$  (°).

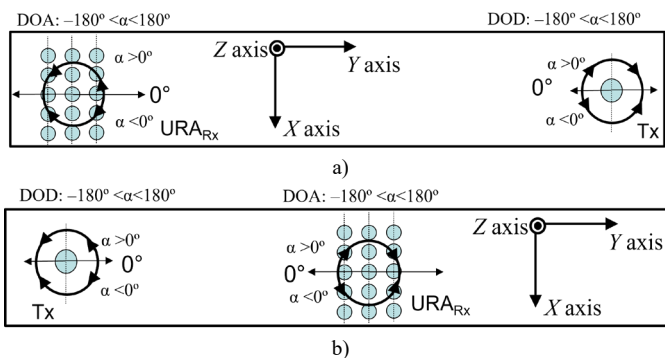


Fig. 18. Reference for the azimuth angle calculation: a) for scenarios 1, 2 and for positions 3-4 of scenarios 3 and 4, b) for positions 1-2 of scenarios 3 and 4.

In Tables XI-XIV the AS results for scenario 1 to scenario 4 are shown. In all cases the AS of the elevation angle is much smaller than the azimuth AS; this conclusion agrees with the result shown in [16] for one Rx position. This difference between the AS of the elevation and azimuth angles is because almost all elevation angles of departure and arrival are close to  $90^\circ$ . On the contrary, three main groups in the azimuth angles are observed: rays with azimuth angles close to  $0^\circ$ , close to  $180^\circ$  and close to  $-180^\circ$ . The first group is composed of the direct ray and those rays coming from the walls and their elements; such elements are placed at the sides of the Tx and Rx and consequently the rays coming from these elements have azimuth angles in the range  $[-50^\circ, 50^\circ]$ . The second and third group comprise the multiple reflections on the ends of the convoy and those rays coming from the ceiling and floor; depending on the location of the Tx and Rx and the type of angle, departure or arrival, each ray of these groups has an azimuth angle the close to either  $180^\circ$  or  $-180^\circ$ .

In scenarios 1 and 2, a trend in the elevation AS is observed: the larger the Tx-Rx distance the smaller the elevation AS. As the Tx moves away from the Rx, the elevation angles of the rays coming from the floor and ceiling become closer to the elevation angles of the rays in the azimuthal plane. The azimuth AS does not follow a clear trend with respect to the distance; moreover, no significant differences are observed between the standing and seated situations; large values are found in both cases.

TABLE XI

ANGULAR SPREAD PARAMETER FOR SCENARIO 1. THRESHOLD 20 DB.				
Position	AS $\theta_{TX}$ ( $^\circ$ )	AS $\theta_{RX}$ ( $^\circ$ )	AS $\phi_{TX}$ ( $^\circ$ )	AS $\phi_{RX}$ ( $^\circ$ )
1	3.88	5.39	26.85	73.23
2	2.98	3.64	25.40	61.97
3	3.91	4.25	10.25	68.92
4	4.67	4.60	24.63	46.35
5	2.80	2.70	45.13	68.41
6	3.17	3.26	44.67	67.79
7	2.08	2.20	52.72	70.87
8	1.51	1.80	63.23	64.48

TABLE XII

ANGULAR SPREAD PARAMETER FOR SCENARIO 2. THRESHOLD 20 DB.				
Position	AS $\theta_{TX}$ ( $^\circ$ )	AS $\theta_{RX}$ ( $^\circ$ )	AS $\phi_{TX}$ ( $^\circ$ )	AS $\phi_{RX}$ ( $^\circ$ )
1	2.66	7.00	31.66	49.20
2	2.72	5.47	24.82	61.71
3	2.90	4.07	10.19	66.77
4	3.03	3.12	38.18	63.08
5	2.54	2.32	53.19	54.66
6	2.00	1.99	74.75	69.16

TABLE XIII

ANGULAR SPREAD PARAMETER FOR SCENARIO 3. THRESHOLD 20 DB.				
Position	AS $\theta_{TX}$ ( $^\circ$ )	AS $\theta_{RX}$ ( $^\circ$ )	AS $\phi_{TX}$ ( $^\circ$ )	AS $\phi_{RX}$ ( $^\circ$ )
1	4.92	5.12	40.17	33.77
2	4.75	6.13	25.40	31.84
3	4.44	5.55	25.61	31.99
4	5.00	4.96	16.49	34.74

TABLE XIV

ANGULAR SPREAD PARAMETER FOR SCENARIO 4. THRESHOLD 20 DB.				
Position	AS $\theta_{TX}$ ( $^\circ$ )	AS $\theta_{RX}$ ( $^\circ$ )	AS $\phi_{TX}$ ( $^\circ$ )	AS $\phi_{RX}$ ( $^\circ$ )
1	5.01	7.32	15.42	22.15
2	3.16	6.85	26.37	34.24
3	2.95	6.63	19.87	35.22
4	7.81	8.23	7.13	24.58

## V. CONCLUSIONS

In this work the wireless channel has been analyzed in an intra-wagon environment between 25 and 40 GHz using a ray-tracing simulation tool. The measured RMS DS, mean delay, and PL have been used to assess the accuracy of the ray tracer; good levels of accuracy have been reached, in the RMS DS 17 out of 22 positions achieved an accuracy above 70%, in the mean delay all positions achieved an accuracy above 80%, and in the PL estimation 19 out of 22 positions a difference below 3 dB. Several parameters, of difficult extraction from the measurements, have been obtained from the simulator. The paths of the components, the contribution to the total power and the angular spread have been studied. The ends of the convoy, the walls and the elements present in the walls are the main contributors to the multipath propagation. When the Tx imitates a standing passenger most of the components have elevation angles close to  $90^\circ$ , since both the passenger and the access point have similar heights. In general, the larger the Tx-Rx distance the smaller the elevation angular spread. High spreads in the azimuth angles have been found in all configurations; no evident trend in the azimuth angles with respect to the distance has been observed.

The analysis has been performed in an empty convoy; in an actual situation the passengers will affect the multipath propagation. In future works, the effect of the passengers will be assessed using the tuned ray-tracing tool.

## ACKNOWLEDGMENTS

The authors would like to thank the staff of FGV who have facilitated the realization of the measurements campaign, in particular J. Iserte Villalba and F. M. Brox López.

## REFERENCES

- [1] K. Guan et al., "5G Channel Models for Railway Use Cases at mmWave Band and the Path Towards Terahertz," *IEEE Intelligent Transportation Systems Magazine*, vol. 13, no. 3, pp. 146-155, Fall 2021, doi: 10.1109/MITS.2019.2926371.
- [2] A. H. Sodhro, G. H. Sodhro, M. Guizani, S. Pirbhulal and A. Boukerche, "AI-Enabled Reliable Channel Modeling Architecture for Fog Computing Vehicular Networks," *IEEE Wireless Communications*, vol. 27, no. 2, pp. 14-21, April 2020, doi: 10.1109/MWC.001.1900311
- [3] T. Zhou, H. Li, Y. Wang, L. Liu and C. Tao, "Channel Modeling for Future High-Speed Railway Communication Systems: A Survey," *IEEE Access*, vol. 7, pp. 52818-52826, 2019, doi: 10.1109/ACCESS.2019.2912408.
- [4] J. M. García-Loygorri, C. Briso, I. Arnedo, C. Calvo, M. A. G. Laso, D. He, F. Jiménez and V. González, "Wideband channel modeling for mm-wave inside trains for 5G-related applications," *Wireless Communications and Mobile Computing*, 2018.
- [5] L. Rubio, V. M. Rodrigo-Peñarrocha, J.-M. Molina-García-Pardo, L. Juan-Llácer, J. Pascual-García, J. Reig and C. Sanchis-Borras, "Millimeter Wave Channel Measurements in an Intra-Wagon Environment," *IEEE Trans. Veh. Technol.*, vol. 68, n° 12, pp. 12427-12431, 2019.
- [6] World Radiocommunication Conference 2015 (WRC-15), Geneva, Switzerland, 2-27 November 2015. [Online]. Available: <https://www.itu.int/en/ITU-R/conferences/wrc/2015/Pages/default.aspx>. [Accessed on: 28 July 2020].
- [7] World Radiocommunication Conference 2019 (WRC-19), Sharm el-Sheikh, Egypt, 28 October to 22 November 2019. [Online]. Available: <https://www.itu.int/en/ITU-R/conferences/wrc/2019/Pages/default.aspx>. [Accessed on: 28 July 2020].
- [8] J. M. García-Loygorri, C. Briso and A. P. Yuste, "Saleh-Valenzuela modelization and clustering information for a mmwave intra-train channel," *2019 13th European Conference on Antennas and Propagation (EuCAP)*, Krakow, 2019.
- [9] M. Soliman, P. Unterhuber and D. Gera, "First analysis of inside Train communication with ITS-G5 measurement data," *International Symposium on Wireless Communication Systems (ISWCS)*, Poznan, 2016.
- [10] I. Val, A. Arriola, P. M. Rodriguez, A. Gonzalez-Plaza, D. Alonso, L. Zhang, C. Briso, J. Moreno, C. R. Sánchez, E. Echeverria and J. Goikoetxea, "Wireless channel measurements and modeling for TCMS communications in metro environments," *2017 11th European Conference on Antennas and Propagation (EUCAP)*, Paris, 2017.
- [11] C. S. Borrás, J. Molina-García-Pardo, L. Rubio, J. Pascual-García, V. M. Rodrigo-Peñarrocha, L. Juan-Llacer and J. Reig, "Millimeter Wave MISO-OFDM Transmissions in an Intra-Wagon Environment," *IEEE Trans. Intell. Transp. Syst.*, pp. 1-10, 2020.
- [12] F. Challita, V. M. Rodrigo-Peñarrocha, L. Rubio, J. Reig, L. Juan-Llácer, J. Pascual-García, J. Molina-García-Pardo, M. Liénard and D. P. Gaillot, "On the Contribution of Dense Multipath Components in an Intra wagon Environment for 5G mmW Massive MIMO Channels," *IEEE Antennas Wireless Propag. Lett.*, vol. 18, n° 12, pp. 2483-2487, 2019.
- [13] Z. Yun and M. F. Iskander, "Ray Tracing for Radio Propagation Modeling: Principles and Applications," *IEEE Access*, vol. 3, pp. 1089-1100, 2015.
- [14] K. Li, D. He, K. Guan, B. Ai, Z. Zhong, L. Tian and J. Dou, "Efficient environment model for intra-wagon millimeter wave ray-tracing simulation," *IEEE International Symposium on Antennas and Propagation & USNC/URSI National Radio Science Meeting*, San Diego, CA, 2017.
- [15] K. Guan, B. Peng, D. He, J. M. Eckhardt, S. Rey, B. Ai, Z. Zhong and T. Kürner, "Channel Characterization for Intra-Wagon Communication at 60 and 300 GHz Bands," *IEEE Trans. Veh. Technol.*, vol. 68, n° 6, pp. 5193-5207, 2019.
- [16] D. He, K. Guan, J. M. García-Loygorri, B. Ai, X. Wang, C. Zheng, C. Briso-Rodríguez and Z. Zhong, "Channel Characterization and Hybrid Modeling for Millimeter-Wave Communications in Metro Train," *IEEE Trans. Veh. Technol.*, vol. 69, n° 11, pp. 12408-12417, 2020.
- [17] D. He, B. Ai, K. Guan, J. M. García-Loygorri, L. Tian, Z. Zhong and A. Hrovat, "Influence of Typical Railway Objects in a mmWave Propagation Channel," *IEEE Trans. Veh. Technol.*, vol. 67, n° 4, pp. 2880-2892, 2018.
- [18] A. Molisch, "Wireless Communications," 2nd ed., Hoboken, NJ, USA: Wiley, 2010.
- [19] M. Martínez-Ingles, D. P. Gaillot, J. Pascual-García, J. Molina-García-Pardo, M. Liénard and J. Rodríguez, "Deterministic and Experimental Indoor mmW Channel Modeling," *IEEE Antennas Wireless Propag. Lett.*, vol. 13, pp. 1047-1050, 2014.
- [20] V. Degli-Esposti, F. Fuschini, E. M. Vitucci and G. Falciasecca, "Measurement and Modelling of Scattering From Buildings," *IEEE Trans. Antennas Propag.*, vol. 55, n° 1, pp. 143-153, 2007.
- [21] C. A. Balanis, "Advanced Engineering Electromagnetics," John Wiley and Sons, 1989.
- [22] L. Possenti, J. Pascual-García, V. Degli-Esposti, A. Lozano-Guerrero, M. Barbiroli, M. Martínez-Ingles, F. Fuschini, J. Rodríguez, E. Vitucci and J. Molina-García-Pardo, "Improved Fabry-Pérot Electromagnetic Material Characterization: Application and Results," *Radio Science*, vol. 55, 2020.
- [23] Recommendation ITU-R P.1238-7 Propagation data and prediction methods for the planning of indoor radiocommunication systems and radio local area networks in the frequency range 900 MHz to 100 GHz, 02/2012.
- [24] J. Järveläinen and K. Haneda, "Sixty gigahertz indoor radio wave propagation prediction method based on full scattering model," in *Radio Science*, vol. 49, no. 4, pp. 293-305, April 2014, doi: 10.1002/2013RS005290.
- [25] N. Reyes, F. Casado, V. Tapia, C. Jarufe, R. Finger and L. Bronfman, "Complex dielectric permittivity of engineering and 3D-printing polymers at Q-band," *Journal of Infrared, Millimeter, and Terahertz Waves*, vol. 39, n° 11, pp. 1140-1147, 2018.



**Juan Pascual-García** was born in Castellón, Spain, in 1975. He received the degree in telecommunications engineer from the Technical University of Valencia (UPV), Valencia, Spain, in 2001, and the Ph.D. degree in communications engineering from the Universidad Politécnica de Cartagena (UPCT), Cartagena, Spain, in 2010. In 2003, he joined the Communications and Information Technologies Department, UPCT, as a Research Assistant, and then as an Associated Professor. In 2009, he joined the SiCoMo Research Group, UPCT, where he is currently developing his research tasks. His research interests include radio wave propagation, ray tracing techniques, and radio channel propagation models.



**Lorenzo Rubio** (Senior Member, IEEE) was born in El Balletero, Albacete, Spain, in 1971. He received the degree in telecommunication engineering and the Ph.D. degree from the Universitat Politècnica de València (UPV), Spain, in 1996 and 2004, respectively. In 1996, he joined the Communications Department, UPV, where he is currently a Full Professor of wireless and radio communications. He is also a member of the Electromagnetic Radiation Group (ERG), Telecommunications and Multimedia Applications Research Institute (iTEAM). His main research interests are related to wireless communications, radiowave propagation, measurement and mobile time-varying channels modeling in vehicular applications, UWB communication systems, multiple-input and multiple-output (MIMO) systems, equalization techniques in digital wireless systems, and mmWave propagation. He was awarded by the Ericsson Mobile Communications Prize from the Spanish Telecommunications Engineer Association for his study on urban statistical radio channel characterization applied to wireless Communications.



**Vicent Miquel Rodrigo Peñarrocha** was born in Valencia, Spain, in 1966. He received the M.S. degree from the Universidad Politécnica de Madrid, Spain, in 1990, and the Ph.D. degree from the Universitat Politècnica de València, Spain, in 2003, in telecommunications engineering. In 1991, he joined the Departamento de Comunicaciones, Universitat Politècnica de València, as a Lecturer. His current interests include radiowave propagation, antenna measurements, instrumentation, virtual instrumentation, and laboratories and any educational activity.



**Leandro Juan Llacer** (Senior Member, IEEE) was born in Albaterra, Spain in 1967. He received the B.S. degree from the Universitat Politècnica de Catalunya in 1993, and the Ph.D. degree from the Universidad Politécnica de Valencia in 1998, in telecommunications engineering. He is currently a Full Professor with the Department of Information Technologies and Communications, Universidad Politécnica de Cartagena, Spain. He has been participating in the COST actions 259, 273, 2100, IC1004, and IRACON. His research activities have focused on the characterization of radio wave propagation in mobile communication systems and the development of radio planning tools based on GIS.



**José-María Molina-García-Pardo** received the degree in telecommunications engineering from the Universidad Politécnica de Valencia, Spain, in 2000, the M.Sc. degree in communication and signal processing from Newcastle upon Tyne, U.K., in September 2001, and the Ph.D. degree in telecommunications and the bachelor's degree in business and administration from the Universidad Politécnica de Cartagena (UPCT), Spain, in 2004 and 2008, respectively. In 2001, he joined the Department of Information Technologies and Communications, Universidad Politécnica de Cartagena, where he has been an Associate Professor, since 2007, a Full Professor accredited in 2012, and a Full Professor since 2016. He is currently a Coordinator of International Relations with the UPCT and leads the SiCoMo Research Group. He is also the Lead Researcher in some national projects and participates actively in the European COST action IC-1004 (Radio Communications for Green Smart Environments). He is the author of more than 75 journals indexed in the JCR, more than 150 international conferences, the author of three book chapters, and owes four patents related to telecommunications. His research activities are centered on radio-communications, propagation, channel modeling and experimental channel sounding in different frequency band (400 MHz to 300 GHz) and technologies (GSM, UMTS, LTE, WiFi, WSN, TETRA, mmW, OFDM, MIMO, BAN, and cognitive radio).



**Concepción Sanchis Borrás** was born in Valencia, Spain, in 1979. She received the degree in telecommunications engineering from the Universidad Politécnica de Valencia (UPV), Spain, in 2004, and the Ph.D. degree in telecommunications from the Universidad Politécnica de Cartagena (UPCT), Cartagena, Spain, in 2012. In 2006, she joined the Department of Technical Sciences of Universidad Católica San Antonio de Murcia (UCAM), where she is currently an Associated Professor. Her research interests include the signal processing techniques for MIMO and radio wave propagation.



**Juan Reig** (Senior Member, IEEE) received the Ph.D. degree from the Universitat Politècnica de València (UPV), Spain, in 2000. He has been a Faculty Member with the Department of Communications, UPV, since 1994, where he is currently a Full Professor of telecommunication engineering. He is also a member of the Electromagnetic Radiation Group (GRE), Institute of Telecommunications and Multimedia Applications (iTEAM). His areas of interests include fading theory, diversity, ultrawide band (UWB) systems, vehicular communications, and millimeter wave (mmWave) propagation.